# Invited Review

*Toxicologic Pathology*, 43: 633-650, 2015

ISSN: 0192-6233 print / 1533-1601 online
DOI: 10.1177/0192623314568390

# Practical Applications of *in Vivo* and *ex Vivo* MRI in Toxicologic Pathology Using a Novel High-performance Compact MRI System

Catherine Tempel-Brami[1], Yael S. Schiffenbauer[1], Abraham Nyska[2], Nati Ezov[3], Itai Spector[3], Rinat Abramovitch[4], and Robert R. Maronpot[5]

[1]*Aspect Imaging, Shoham, Israel*
[2]*Tel Aviv University and Consultant in Toxicologic Pathology, Timrat, Tel Aviv, Israel*
[3]*Harlan Biotech Israel, Nes Ziona, Israel*
[4]*Hadassah Hebrew University Medical Center, Jerusalem, Israel*
[5]*Maronpot Consulting, LLC, Raleigh, North Carolina, USA*

Abstract

Magnetic resonance imaging (MRI) is widely used in preclinical research and drug development and is a powerful noninvasive method for assessment of phenotypes and therapeutic efficacy in murine models of disease. *In vivo* MRI provides an opportunity for longitudinal evaluation of tissue changes and phenotypic expression in experimental animal models. *Ex vivo* MRI of fixed samples permits a thorough examination of multiple digital slices while leaving the specimen intact for subsequent conventional hematoxylin and eosin (H&E) histology. With the advent of new compact MRI systems that are designed to operate in most conventional labs without the cost, complexity, and infrastructure needs of conventional MRI systems, the possibility of MRI becoming a practical modality is now viable. The purpose of this study was to investigate the capabilities of a new compact, high-performance MRI platform (M2™; Aspect Imaging, Israel) as it relates to preclinical toxicology studies. This overview will provide examples of major organ system pathologies with an emphasis on how compact MRI can serve as an important adjunct to conventional pathology by nondestructively providing 3-dimensional (3-D) digital data sets, detailed morphological insights, and quantitative information. Comparative data using compact MRI for both *in vivo* and *ex vivo* are provided as well as validation using conventional H&E.

*Keywords:* MRI; *ex vivo*; *in vivo*; magnetic resonance histology (MRH); toxicology; pathology; preclinical imaging.

## Introduction

Magnetic resonance imaging (MRI) is a powerful method for noninvasive *in vivo* assessment in preclinical research, as well as drug development and for phenotyping small animal models of disease. In preclinical studies, *in vivo* MRI can be used in longitudinal studies to monitor progression, regression, and therapeutic responses of diseases noninvasively. As such, there is no longer a need to sacrifice animals at interim time points and the same animal can be imaged and reimaged longitudinally thereby becoming its own control. In 1993, a novel approach of using MRI on fixed tissue specimens and perfusion-fixed laboratory animals to generate 3-dimensional (3-D) digital images of the samples was introduced and the term magnetic resonance histology (MRH) was coined (Johnson et al. 1993). This was followed by several neurotoxicology publications (Lester et al. 1999, 2000; Maronpot,Sills, and Johnson 2004; Morgan, Horsfield, and Steward 2004; Sills et al. 2004) that clearly demonstrated the value of MRH as a complementary adjunct to conventional histopathology. However, up until this time, widespread adoption of MRH has been hampered by the high purchase costs of conventional superconducting MRI systems, in addition to the significant siting and installation, operation, and ongoing maintenance costs of these MRI systems. In addition, there are significant safety concerns and complexities associated with operating superconducting MRI systems, which require dedicated technical staff with specific MR-based physics expertise to operate the instruments and their complicated sequences and imaging protocols.

The author(s) declared no potential conflicts of interest with respect to the research, authorship, and/or publication of this article.

The author(s) received no financial support for the research, authorship, and/or publication of this article.

Address correspondence to: Yael S. Schiffenbauer, 27 Shaked St. Industrial Area Hevel Modi'in, P.O. Box 926, Shoaham 608500, Israel; e-mail: yael@aspectimaging.com.

Abbreviations: 2-D, 2-dimensional; 3-D, 3-dimensional; AKI, acute kidney injury; COPD, chronic obstructive pulmonary disease; FA, flip angle; FOV, field of view; H&E, haematoxylin and eosin; LPS, lipopolysaccharide; MIP, maximal intensity projection; MRI, magnetic resonance imaging; MRH, magnetic resonance histology; RF, radiofrequency; T1, spin–lattice relaxation time; T2, spin–spin relaxation time; TE, echo time; TR, repetition time.

A new compact, high-performance MRI platform (M2™; Aspect Imaging, Israel) has been developed using a novel magnet design and set of associated software and application-based approaches that reduce the cost and complexity of conventional systems. This new MRI platform provides the opportunity for pathologists with no prior MR or imaging expertise to obtain diagnostic-quality *in vivo* MRI and *ex vivo* MRH images of experimental rodents, thereby greatly enhancing conventional histopathology in preclinical toxicology studies and in the development of rodent models of human disease (Geninatti-Crich et al. 2011; Schmid et al. 2013). Unlike superconducting MRI systems, this system is portable and self-shielded so it can be placed in most laboratories or research facilities and does not require a specially shielded room, cryogens or coolants, or dedicated electrical or plumbing supply. In addition, this system has dedicated software and hardware with preprogrammed protocols and sample handling systems to easily allow pathologists to perform high-throughput imaging of animals *in vivo* or of fixed samples *ex vivo*. The advantages of this new system are the ability for longitudinally monitoring disease (*in vivo* MRI) and rapid acquisition of multiple electronic slices of fixed tissue (*ex vivo* MRH), thereby providing 3-D digital morphologically detailed data of an entire target organ while leaving the specimen intact for follow-on conventional histopathology. This leads to a more comprehensive assessment of toxicological effects and disease progression in contrast to the limited number of 2-dimensional (2-D) tissue slices afforded by conventional histopathology.

The purpose of this article is to describe the utility of this new compact MRI platform in preclinical toxicologic pathology by providing examples of practical toxicology and experimental biology applications.

FIGURE 1.—Presentation of the new compact M2™ high-performance magnetic resonance imaging (MRI) platform for *in vivo* and *ex vivo* MRI-based histology applications (Aspect Imaging, Israel). The M2 system is a compact, high-performance MRI system that uses a permanent magnet, which ensures there is no external magnetic field enabling the system to be operated in most facilities and does not require any shielding, speciality facilities, or cooling and cryogens to maintain the magnetic field. It is equipped with rat and mouse body and head coils. Animals are kept anesthetized with 2% isoflorane in $O_2$ on a specially designed heated bed and physiological signals are monitored throughout the experiment to ensure well-being of the animals. High-resolution *ex vivo* MRH is performed using a 20 mm radiofrequency (RF) coil on the same compact high-performance MRI system. In this configuration, the system allows high-throughput and automatic scanning of up to 10 samples without technician intervention. Briefly, fixed samples are introduced in specially designed disposable capsules that are given a unique bar code. The operator assigns predefined MR protocols to the bar coded sample, according to the organ or pathology under investigation. Up to 10 capsules can then be loaded into the system, which automatically advances, scans, and ejects the capsules one at a time. No intervention is required throughout the process, so samples can be left unattended to be scanned overnight.

## METHODS

### In Vivo *Compact MRI*

*In vivo* MRI was performed using the M2, a compact, high-performance MRI system, equipped with a set of application-specific radiofrequency (RF) coils: 60-mm rat whole body coil, 35-mm mouse whole body coil, in addition to 30-mm and 20-mm rat and mouse head coils, respectively (Figure 1). For *in vivo* imaging, animals were maintained in an anesthetized state with 2% isoflorane in $O_2$ and placed on a specially designed heated bed where physiological signals were monitored throughout the experiment to ensure the animals' well-being. The optimal RF coil was selected for scanning according to the animal model and body part of interest. All experiments were performed in accordance with the guidelines and approval of the Animal Care and Use Committees of the various organizations providing the animal models.

### Ex Vivo *MR-based Histology*

High-resolution *ex vivo* MRH of fixed samples was performed on the same M2 compact MRI system (Figure 1) equipped with a 20-mm RF coil and a custom-designed automated feeding and scanning mechanism for high-throughput pathological imaging. In this configuration, the compact MRI system allows for high-throughput, automated scanning of up to 10 fixed samples without technician intervention. Briefly, fixed samples are placed into specially designed disposable capsules that are given a unique bar code. The operator assigns predefined MR protocols from a library of organ- and pathology-specific protocols. The


FIGURE 2.—*In vivo* longitudinal study of acute kidney injury (AKI) in mouse. Loss of contrast between cortex and medulla as well as kidney enlargement were most prominent 3 (B) and 8 (C) days following induction of AKI. By day 15 (D), contrasts between cortex and medulla recovered and kidney size was back to normal. MRI acquisition parameters include fast spin echo with repetition time = 3000 ms, echo time = 80 ms, field of view = 60 mm, slice thickness = 1 mm, matrix = 256 × 256, and acquisition time = 10 min.

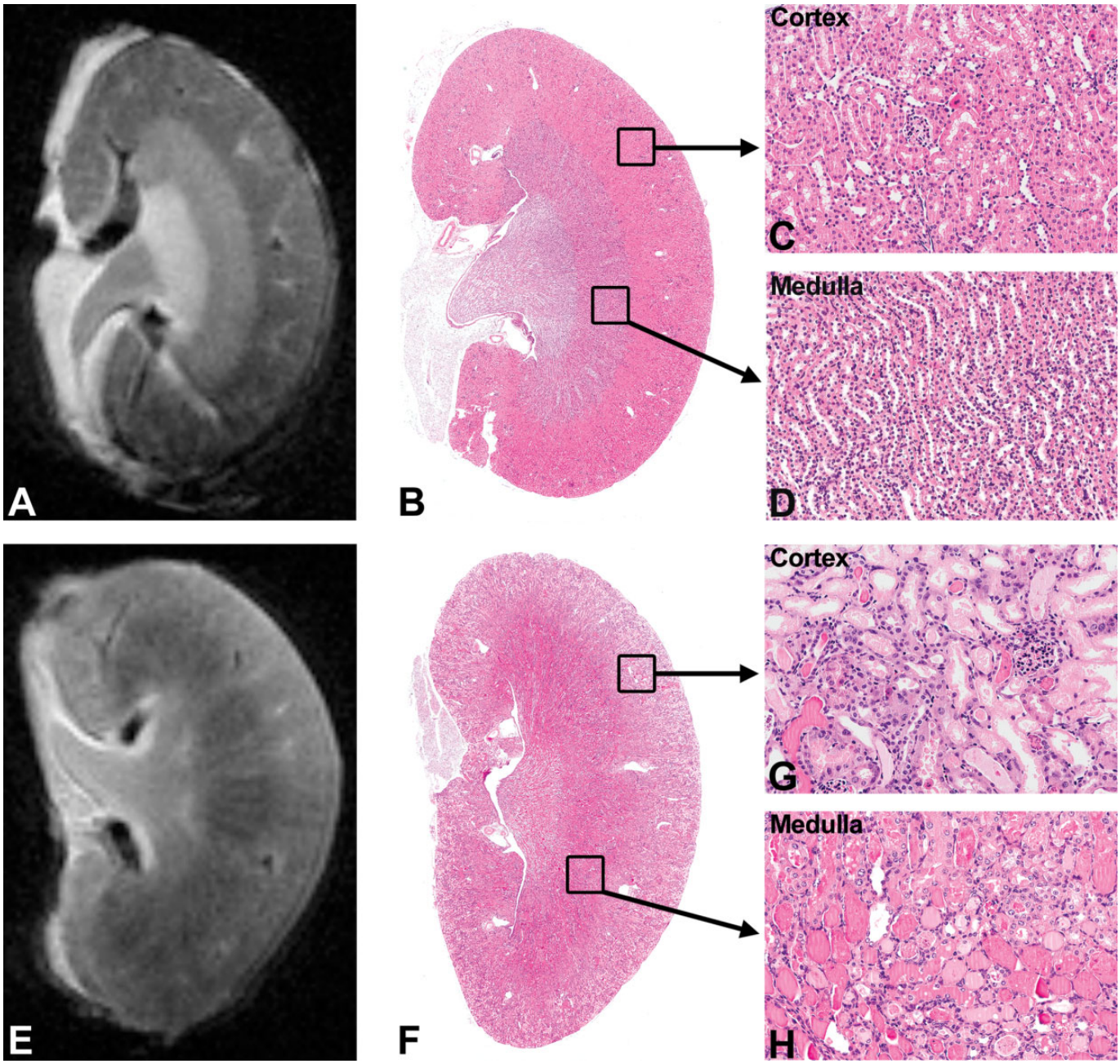


FIGURE 3.—*Ex vivo* magnetic resonance histology (MRH) and hematoxylin and eosin (H&E) histopathology of control and AKI affected kidney. *Ex vivo* MRH of control kidney (A) with excellent distinction between cortex and medulla confirmed by the normal appearance of these regions in H&E histology sections (B, C, and D). *Ex vivo* MRH of the affected kidney (E) with loss of regional distinction (cortex to medulla) and H&E histology (F) with tubular necrosis in the cortex (G) and tubular dilation with protein casts in the medulla (H). MRI acquisition parameters include fast spin echo with repetition time = 2,500 ms, echo time = 44 ms, field of view = 30 mm, slice thickness = 0.5 mm, matrix = 256 × 252, and acquisition time = 56 min.

appropriate protocol is associated with the bar-coded sample, according to the organ or pathology of interest. Up to 10 capsules, each with their own application-specific imaging protocol can then be loaded into the system, which automatically advances the sample into the MRI unit. The specified imaging protocol is executed, the capsule is ejected after imaging, and the next sample is then automatically advanced and its unique imaging protocol is executed. The process continues automatically until all 10 samples are imaged. Once loaded into capsules and given a bar code, no technician intervention or supervision is required throughout the imaging process. As such, samples can be left unattended to be scanned overnight, for example, so that the system can be used during the day for *in vivo* imaging or to run additional capsules during the day. Effectively, throughput can be maximized so that the system can be used 24 hr per day.

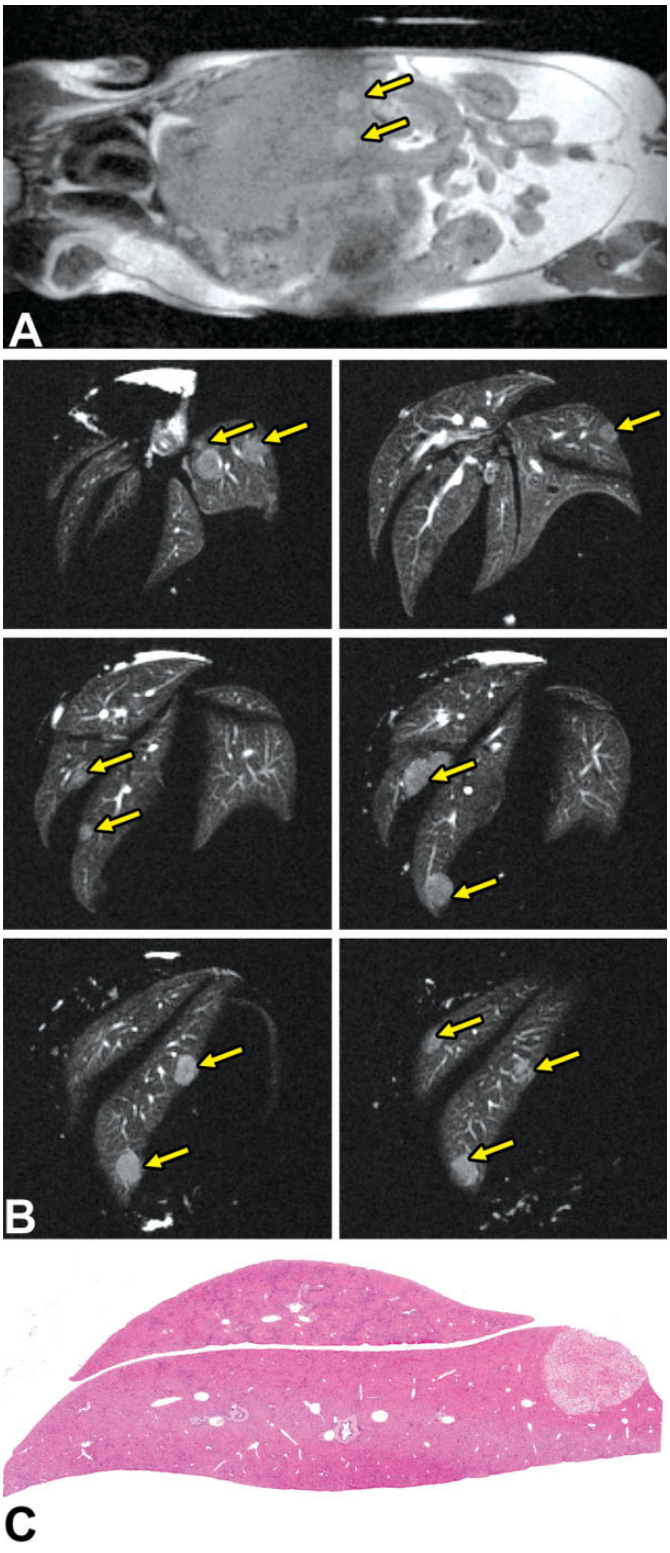


FIGURE 4.—Focal liver lesions in Mdr (−/−) mice. (A) *In vivo* magnetic resonance imaging (MRI) of a 14-month-old Mdr (−/−) mouse showing multiple focal lesions in the liver (arrows). MRI acquisition parameters include spin echo with repetition time = 450 ms, echo time = 11.5 ms, field of view = 70 mm, matrix = 256 × 256, slice thickness = 1 mm, and acquisition time 3.50 min. (B) *Ex vivo* magnetic resonance histology (MRH) of the fixed liver.

Samples were fixed using conventional immersion fixation techniques, transferred to phosphate-buffered saline or saline for 24 hr, and then into an MR transparent solution (Fluorinert FC, 3M, USA) to avoid tissue dehydration.

### *Image Processing and Quantification*

Renderings, movies, segmentation, and volumetric quantification of the digital 3-D MRI data were performed using VivoQuant® (InviCRO, Boston), an extensive image processing and analysis software package that is fully integrated into the M2 imaging system. It allows for easy quantification of 2-D and 3-D MR-based images for both *in vivo* and *ex vivo* samples in addition to coregistration of images from multiple imaging modalities. Images can be imported from nearly every preclinical imaging modality and manufacturer.

### *Histopathology*

As MRI is a noninvasive, nondestructive imaging modality, conventional histopathological analysis of the same fixed organs was done following *ex vivo* MRI scanning. Following *ex vivo* MRI, the scanned specimens were transferred back to the fixative solution and then embedded in paraffin, sectioned, and stained with hematoxylin and eosin (H&E). *Ex vivo* MRI-based images and histopathology of the same samples were then analyzed and compared. The MRI images define the location, size, and number of lesions while definitive lesion diagnoses are always based on conventional histopathology.

### *Terminology*

As with most specialized areas of knowledge and unique technologies, invariably there is a technology-related lexicon. Sample orientation refers to the orientation of the animal or sample, and like the clinical situation, the three main orientation views are sagittal, coronal, and axial views. MRI of live animals is referred to as *in vivo* imaging, while MRI on fixed specimens is referred to as *ex vivo* imaging. By changing the imaging parameters such as duration and timing of applied magnetic fields and RF pulses, MRI provides digital slices of the sample with a certain resolution and contrast that could be considered a digital "stain." The two most common MRI "stains" are referred to as spin–lattice relaxation time (T1) and spin–spin relaxation time (T2; Loeffler and Oppelt 1981; Smith 1985). Data are acquired in 3-D and can be visually presented as a collection of contiguous or noncontiguous slices. These can be viewed as independent images or strung together and viewed as an animated video. By adjusting the density of

FIGURE 4.—(Continued) Different MR slices of the fixed liver with many focal lesions (arrows). MRI acquisition parameters include fast spin echo with repetition time = 5,870 ms, echo time = 80 ms, field of view = 40 mm, ST = 0.7 mm, matrix = 256 × 256, and acquisition time = 78.4 min. (C) Histopathology (hematoxylin and eosin [H&E]) of the liver showing the focal fatty change characteristics of the lesions.

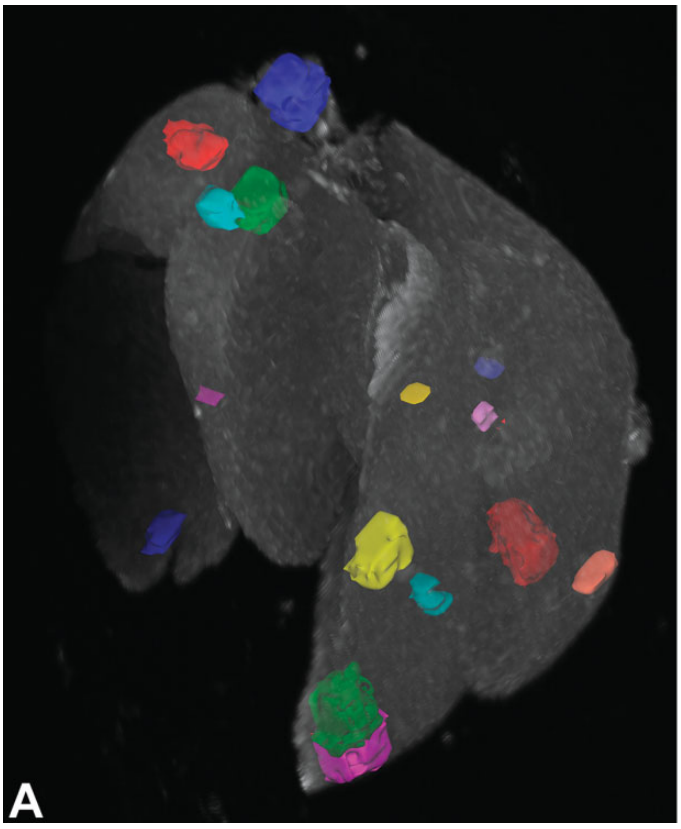


| ROI | Color | Voxels | Volume mm³ |
|---|---|---|---|
| 1 | red | 3931 | 2.27461 |
| 2 | green | 6248 | 3.61531 |
| 3 | blue | 7211 | 4.17253 |
| 4 | cyan | 2191 | 1.26779 |
| 5 | magenta | 13717 | 7.93713 |
| 6 | yellow | 5619 | 3.25135 |
| 7 | dark red | 15125 | 8.75184 |
| 8 | dark green | 13156 | 7.61251 |
| 9 | dark blue | 1484 | 0.858693 |
| 10 | dark cyan | 1618 | 0.93623 |
| 11 | dark magenta | 90 | 0.0520771 |
| 12 | tomato | 1183 | 0.684524 |
| 13 | gold | 116 | 0.0671216 |
| 14 | midnight blue | 420 | 0.243026 |
| 15 | orchid | 632 | 0.365697 |

B

FIGURE 5.—3-Dimensional (3-D) presentation of a fixed liver with multiple focal fatty change lesions. (A) Maximal intensity projection 3-D magnetic resonance (MR) rendering of the whole fixed liver showing the segmented focal lesions. Segmentation was performed using VivoQuant® global/connected/neighboring thresholding. (B) Table summarizing the volume of each individual lesion.

specific components of a set of MRIs, outer layers can be made partially transparent, allowing visualization of internal structures; this is referred to as a maximal intensity projection (MIP) rendering. Finally, specific tissues or structural components in the slices can be isolated, a process called segmentation. Digitally segmented structures are easily measured, providing a 3-D volume of the segmented item of interest (e.g., a segmented tumor volume).

### *Applications of Compact MRI in Toxicologic Pathology*

Presentation of examples of MRI in toxicologic pathology has been previously reported based on the use of large superconducting MRI systems at various imaging centers and represent proof of principle of the value of MRI in toxicology and toxicologic pathology (Dixon et al. 1988; Maronpot, Sills, and Johnson 2004; Johnson et al. 1993; Johnson et al. 1989; Hanig et al. 2014). As part of the miniaturization of *in vivo* imaging equipment, which is enabling broader access to imaging tools by more biologists and facilities, the M2 compact permanent magnet-based MRI system has enabled such access in the MRI field. As part of an extensive validation project, we collaborated with several investigators to utilize *in vivo* and *ex vivo* compact MRI on various toxicology-relevant animal models. MRI was followed by conventional histopathologic evaluation for comparison and validation and to provide definitive diagnoses. In this article, we provide an overview of the results obtained in several toxicologically relevant biological models of disease induced in mice and rats.

#### *Rhadbomyolysis acute kidney injury in mice*

Acute kidney injury (AKI) is a potential complication of severe rhabdomyolysis. It represents about 7–10% of all cases of AKI in the United States (Bosch, Poch, and Grau 2009). AKI was induced in CB6F1 mice at Hadassah Hebrew University (Jerusalem, Israel) by intramuscular injection of 50% glycerol, at a total dosage of 8 ml/kg; one-half dose was injected into the anterior thigh muscle of each hind leg. Compact MRI and urea blood level measurements were executed on days 0, 3, 8, and 15 following glycerol injections to determine AKI severity (Milman et al. 2013).

Time course changes in renal morphology and corticomedullary differentiation were evaluated *in vivo* on anesthetized mice and *ex vivo* on extracted fixed kidneys using the same M2 compact MRI platform. H&E histology and immunostaining for apoptosis were also performed.

On day 3, changes in MRI contrast compared to control kidney images (Figure 2A) were readily observed in affected kidneys *in vivo* (Figure 2B) as well as *ex vivo* (Figure 3), indicating higher water content in the cortex as a result of edema and cell death manifested as enhanced signal intensity in T2-weighted images. The changes consisted of the loss of

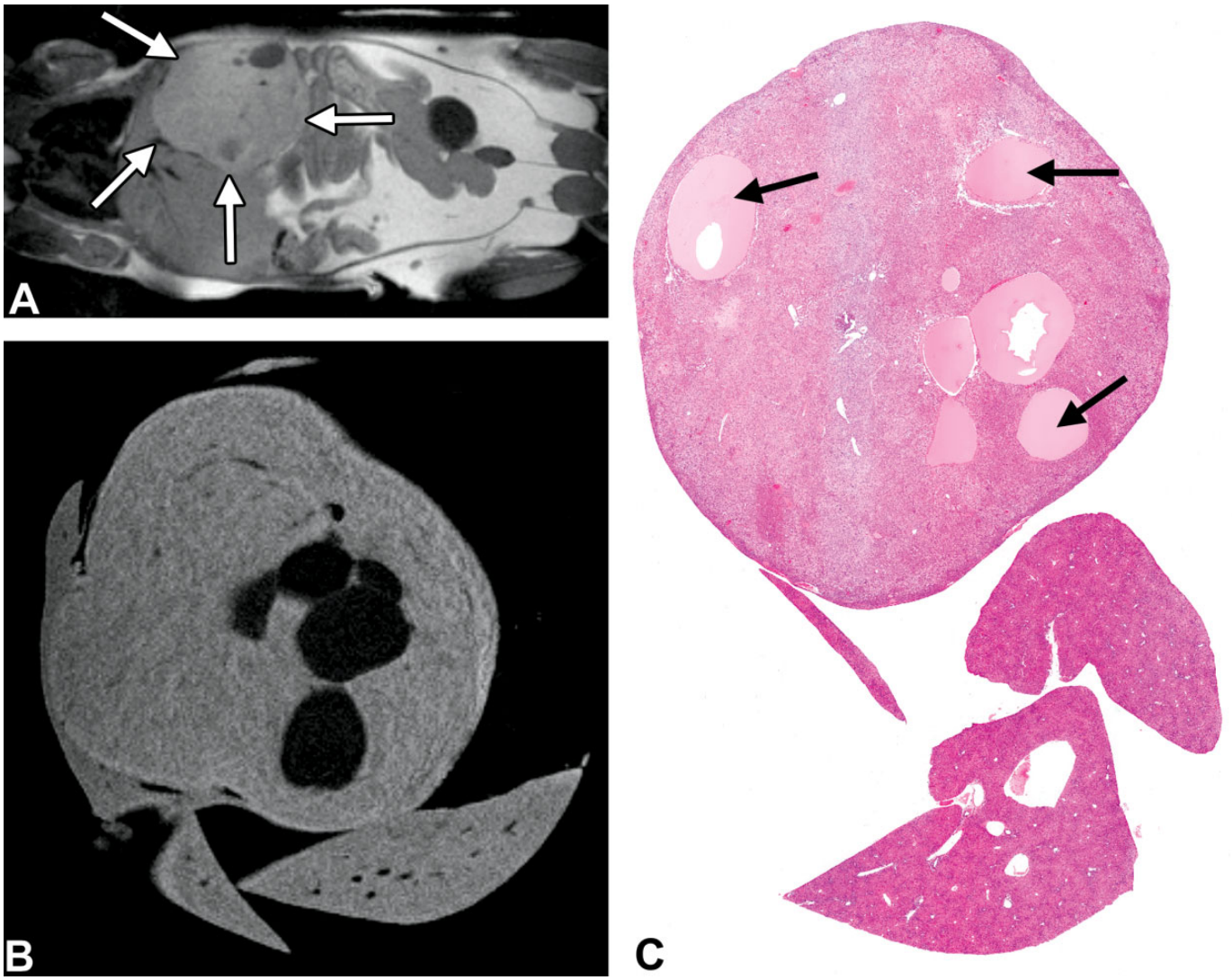


FIGURE 6.—Cystic hepatocarcinoma in Mdr (−/−) mice. (A) *In vivo* magnetic resonance imaging (MRI) from a 14-month-old Mdr (−/−) mouse with a large cystic hepatocellular carcinoma (arrows). MRI acquisition parameters include spin echo with slice thickness = 1 mm, repetition time = 450 ms, echo time = 11.5 ms, field of view = 70 mm, matrix = 256 × 256, and acquisition time = 3.5 min. (B) *Ex vivo* MRI of the formalin-fixed tumor showing dark cystic spaces. MRI acquisition parameters include gradient echo with repetition time = 50 ms, echo time = 7 ms, flip angle = 80°, field of view = 25 mm, slice thickness = 0.3 mm, matrix = 300 × 300, and acquisition time = 133 min. (C) Histopathology (hematoxylin and eosin [H&E]) of the liver containing a large hepatocellular carcinoma with multiple cystic structures (arrows).

regional contrast (cortex to medulla), which was clearly seen in control samples. In addition, the injured kidneys were enlarged. Administration of an MRI contrast agent (Gd-DTPA, Diethylenetriaminepentaacetic acid gadolinium) via tail vein injection revealed delayed filtration and washout, demonstrating renal dysfunction supported by high urea levels in urine (data not shown). Histopathology showed maximal extent of cortical necrosis and medullary hyaline cast formation in injured kidneys 3 days following glycerol injection.

On day 15, *in vivo* MRI confirmed organ recovery both in corticomedullary contrast and size (Figure 2D). Follow-on histopathology confirmed that the necrotic tubules were being replaced by tubular regeneration. The use of *in vivo* M2 compact MRI in this AKI preclinical model demonstrates a useful adjunct to conventional histopathology by permitting the pathologist to follow the progression and regression of renal injury in the same animal longitudinally and to more fully understand the characterization of the disease. The subsequent *ex vivo* MRI provides enhanced image resolution and permits multiple digital slices to create a 3-D morphological assessment of the full target organ without perturbing the sample and thereby allowing conventional follow-on histopathological assessment.

### *Focal hepatic lesions*

Mdr−/− mice, provided by Hadassah Hebrew University (Jerusalem, Israel), are known to develop age-associated

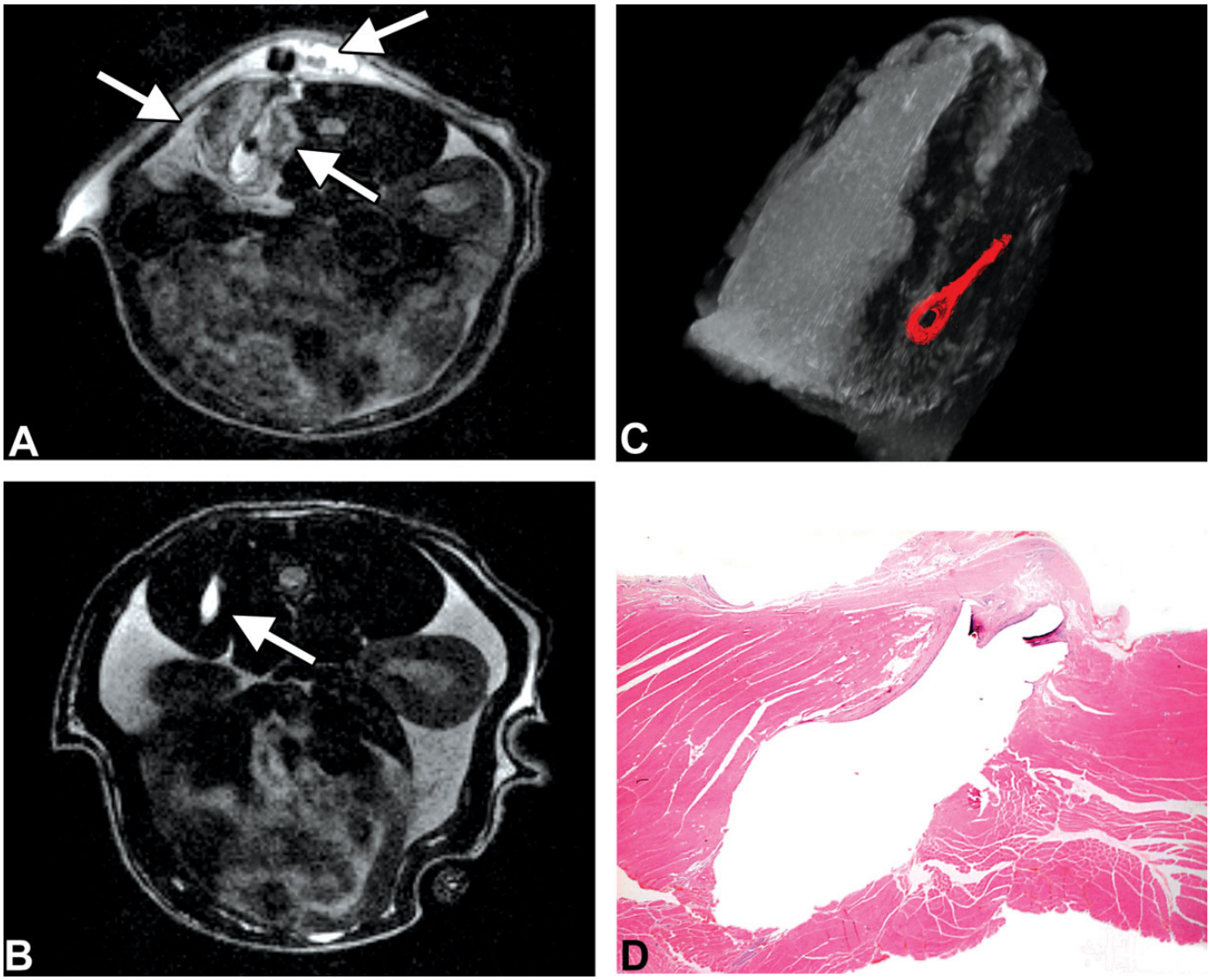


FIGURE 7.—Biodegradable implanted device. A double layer of a 5 × 5 $mm^2$ device was implanted in the right paralumbar muscle of Sprague-Dawley rats. A plastic bead was implanted subcutaneously just over the device to enable accurate localization and follow-up of the implantation site. (A) *In vivo* magnetic resonance imaging (MRI) performed on a rat 5 days after implantation with a diffuse bright signal (arrows) around the device indicating inflammation. (B) Sixty days after implantation, there is recovery (lack of inflammation) around the implanted device (arrow). The bright signal near the tip of the arrow represents the implanted device. MRI acquisition parameters include fast spin echo with repetition time = 4,400 ms, echo time = 80 ms, field of view = 70 mm, slice thickness = 1 mm, matrix = 200 × 192, and acquisition time = 6 min. (C) Maximal intensity projection of the 3-dimensional (3-D) MR rendering of the biopsied formalin-fixed muscle containing the implanted device 60 days after implantation. Segmentation of the device appears in red. The volume of the device is 32.2 $mm^3$. MRI acquisition parameters include gradient echo with repetition time = 50 ms, echo time = 7 ms, flip angle = 80°, field of view = 35 mm, slice thickness = 0.3 mm, matrix = 300 × 300, and acquisition time = 60 min. (D) Histopathology (hematoxylin and eosin [H&E]) of implantation site after 60 days. The cavity left by the extracted device is surrounded by mature thin connective tissue capsule and absence of inflammation.

spontaneous liver lesions (Mauad et al. 1994). Our objective was to detect, count, and measure the volumes of the lesions. *In vivo* MRI detected focal liver lesions in all mice ($n = 6$; Figure 4A). Higher-resolution *ex vivo* MRH evaluation of the livers allowed the identification of several individual focal fatty lesions in some of the mice (Figure 4B and C) and hepatocellular carcinomas in others (Figure 5). The 3-D digital data obtained allowed for digital segmentation and quantification of all individual lesions (Figure 6). In the example shown in Figures 4 and 6, 15 focal lesions were detected, the smallest having a volume of 0.3 $mm^3$. The total lesion mass in this specific case was 42 $mm^3$, representing 2.3% of the total liver mass. The lesions were validated as focal fatty changes by conventional histopathology (Figure 4C). Having received the mice at the

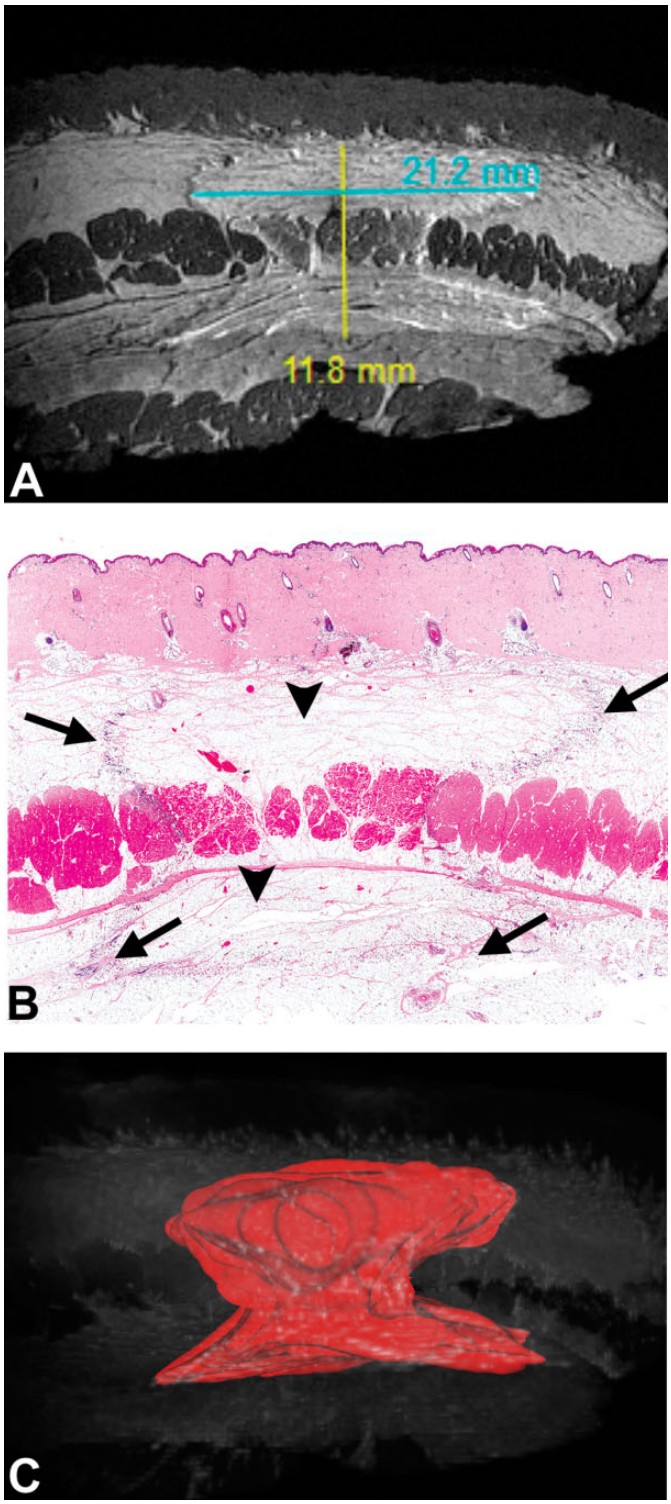


FIGURE 8.—Subcutaneous lesion following drug infusion. The fixed sample is characterized by subcutaneous local toxicity following continuous infusion over 14 days in domestic pig. (A) *Ex vivo* magnetic resonance histology (MRH) slice of the skin biopsy showing the damaged area and (B) the correlating hematoxylin and eosin (H&E) histology slice of the biopsied pig's skin where the lesion is apparent with multifocal areas of fat necrosis and associated inflammation (arrows) and normal adipose tissue (arrow heads). MRI acquisition parameters include gradient echo with repetition time = 50 ms, echo time = 7 ms, flip angle = 80°, field of view = 50 mm, slice thickness = 0.3 mm, matrix = 300 × 300, and acquisition time = 67 min. (C) Maximal intensity projection of the 3-dimensional (3-D) magnetic resonance imaging (MRI)-rendered image of the biopsied skin showing the affected volume segmented.

end of an ongoing study, we were unable to utilize *in vivo* MRI to follow lesion progression over time. However, *ex vivo* MRH was an important contribution at the single time point to conventional histopathology, providing 3-D digital slices through the entire liver and allowing for quantification of multiple individual lesions.

### *Implanted medical devices*

Our vision concerning the future role of MRI in the assessment of biocompatibility evaluation of implanted biomaterials and medical devices can be outlined as follows: In the case of development of novel biomaterials and medical devices, the toxicologic pathologist assesses the safety (biocompatibility) and efficacy (conditions of use) of the implantable materials, which eventually helps to predict their safety after implantation in humans (De Feo et al. 2009; Nyska et al. 2003; Okner et al. 2009; Schuh 2008). The implantation sites are expected to be examined *in vivo* at periodic intervals until the tissue has healed and returned to normal (Northup 1999). Nowadays, when applying microscopic evaluation as an investigative tool to screen for biocompatibility, there is an obvious limit in knowing 3-D structure, potential time-related changes in the size of the device in the tissue, surrounding tissue reaction, as well as progressive absorption and location of the device. MRI is suggested to become a primary tool used for assessing biocompatibility of implanted biodegradable materials, since it allows for longitudinal imaging, without the need for interim sacrifices of animals, 3-D quantification of inflammation *in vivo* caused by the device implantation as well as enabling general 3-D inspection of shape, location, and integrity of the device. The M2 compact MRI system was used to follow tissue reaction to a biodegradable device implanted in the paralumbar muscle of rats (model provided by Harlan Biotech, Israel). The implant was evaluated by *in vivo* compact MRI 5 and 60 days after implantation. Inflammation related to the implantation process, manifested as enhanced signal intensity in T2-weighted images, was detected in the first days after implantation with progressive reduction in the inflammatory process and the biodegradation of the device over time (Figure 7A and B). *In vivo* MRI was able to demonstrate the presence of the device in the paralumbar muscles up to 16 weeks postimplantation. *Ex vivo* MRH of the extracted tissue permitted accurate quantification of device volume and shape (Figure 7C). Conventional H&E evaluation showed the cavity left by the extracted device surrounded by mature connective tissue capsule and confirmed shape and device biocompatibility (Figure 7D). The combination of *in vivo* and *ex vivo* M2 compact MRI with conventional histopathology provided the investigators the ability to

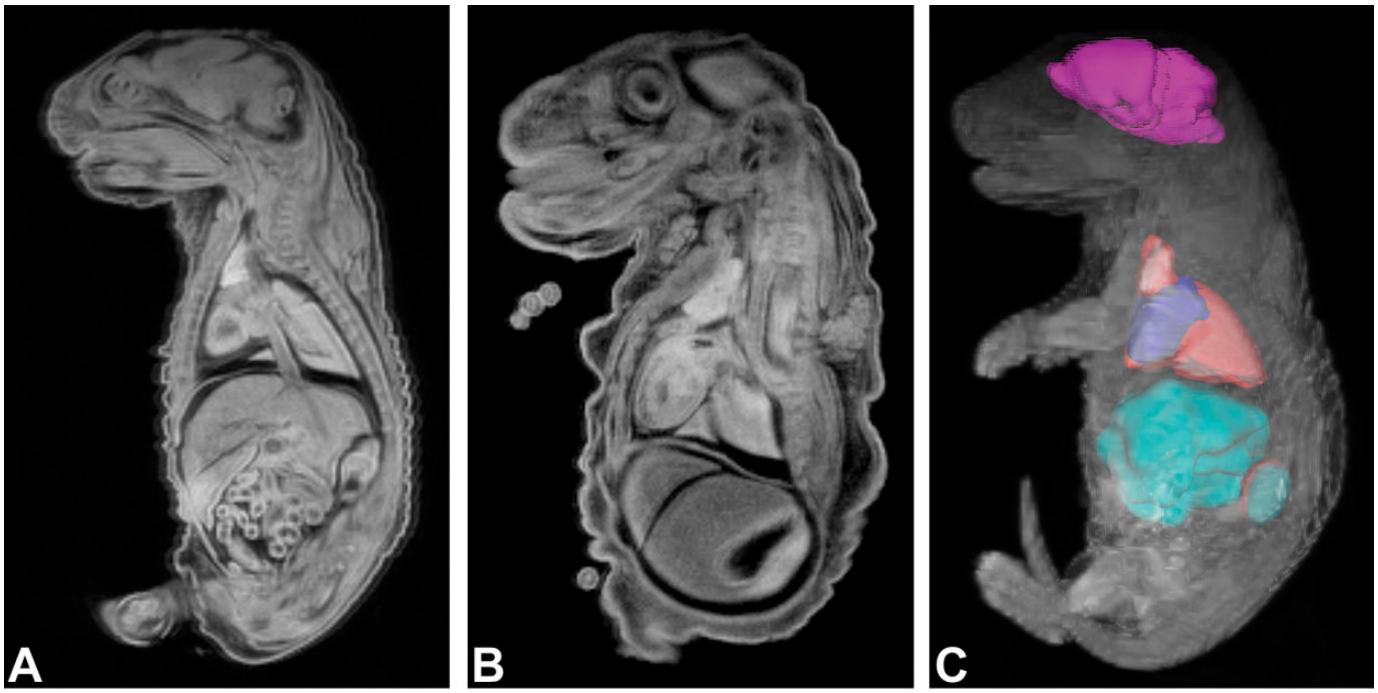


| ROI | Rat | Color | Voxels | Volume mm³ |
|---|---|---|---|---|
| Lungs | rat embryo control E20 | red | 28910 | 97.5713 |
| Heart | rat embryo control E20 | blue | 8218 | 27.7358 |
| Liver | rat embryo control E20 | cyan | 84566 | 285.41 |
| Brain | rat embryo control E20 | magenta | 38770 | 130.849 |
| Left Kidney | rat embryo control E20 | dark red | 3044 | 10.2735 |
| Right Kidney | rat embryo control E20 | dark cyan | 2745 | 9.26438 |

D

FIGURE 9.—*Ex vivo* magnetic resonance imaging (MRI) of control and cyclophosphamide-treated rat embryos. (A) *Ex vivo* MRI of control and (B) cyclophosphamide-treated E20 rat embryos with a hammerhead phenotype. MRI acquisition parameters include gradient echo with repetition time = 50 ms, echo time = 8 ms, flip angle = 80°, field of view = 40 mm, matrix = 300 × 300, slice thickness = 0.3 mm, and acquisition time = 133 min. (C) Maximal intensity projection of the 3-dimensional (3-D) MRI rendering of the control rat embryo with quantified segmented organs presented in the table (D).

dynamically monitor host reaction and implant biocompatibility in the same rat longitudinally and to obtain detailed and quantifiable imaging assessment of the potential toxicological effects of an implantable device in preclinical models.

*Subcutaneous lesions following therapeutic injection*

In the developmental process of novel therapeutics for subcutaneous administration, the toxicologic pathologist assesses the local safety (biocompatibility) of the injectable test compound, which eventually helps to predict the safety of the therapeutic after injection in humans (Nyska et al. 1994; Ramot et al. 2012, 2014). The injection sites are expected to be examined by histopathology, and every component of tissue reaction, like necrosis, inflammation, pigmentation, mineralization, capsule formation, foreign body granuloma, and so on, should be described and graded semiquantitatively (Nyska et al. 2014). When applying histopathology as an investigative tool to learn about local tissue reaction, there is an obvious limit in identifying the 3-D extent and time-related progression of such lesions. *In vivo* MRI can evaluate tissue changes over time and *ex vivo* MRH on skin biopsies can provide a quantitative determination of relative irritancy of different injected formulations.

In our study, *ex vivo* MRH was used to evaluate the local damage of commercial Apo-Go, a therapeutic used as a symptomatic therapy in Parkinson's disease and compared to a newly developed apomorphine formulation ND0701 (Apo-ND) by Neuroderm (Rehovot, Israel). The MRH results were then compared to histopathology.

The experiment was carried out in domestic pigs that underwent 14 days of continuous infusion of the drug formulations.

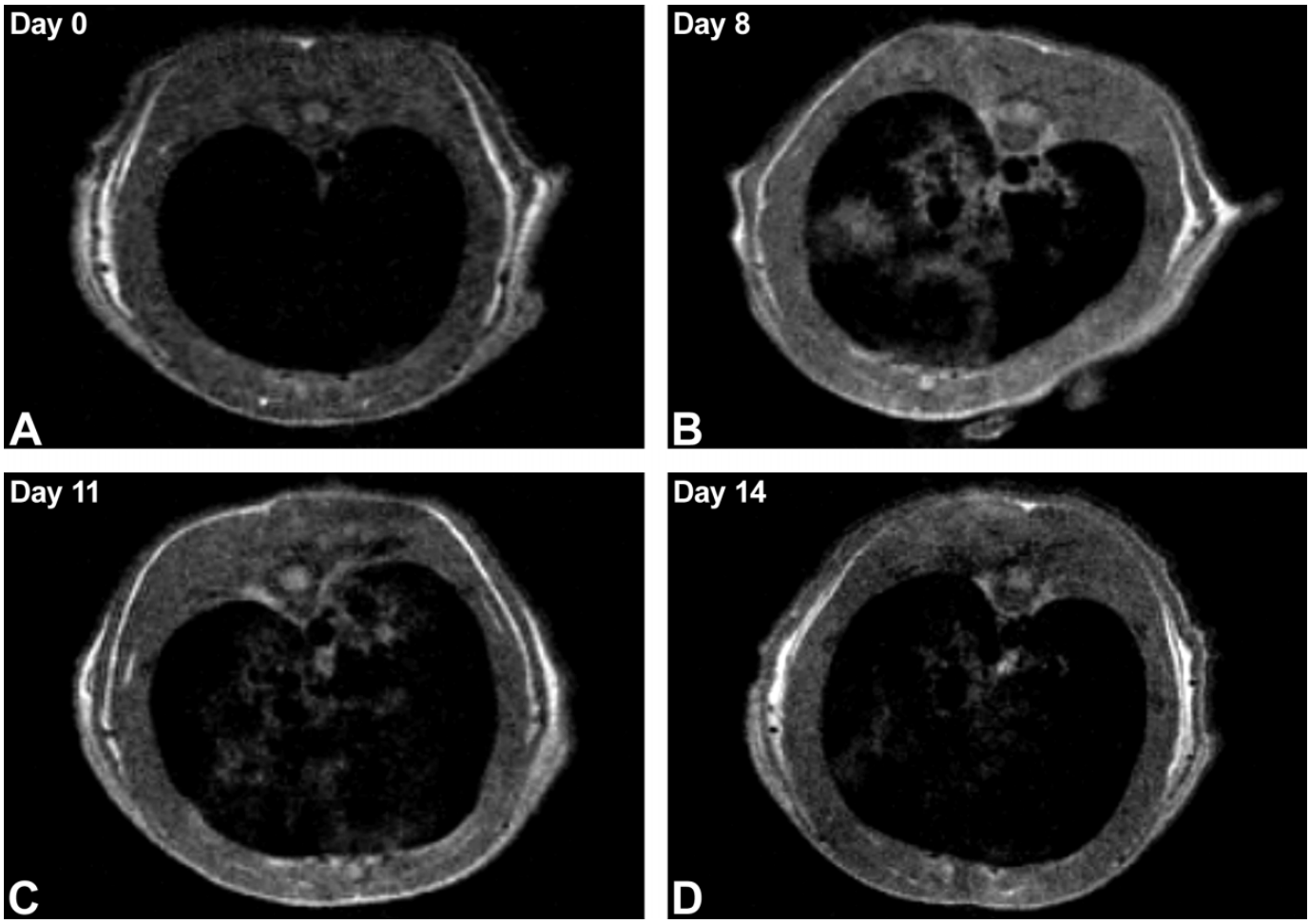


FIGURE 10.—*In vivo* magnetic resonance imaging (MRI) of rat lungs. (A–D) *In vivo* longitudinal follow-up of a rat over 14 days following intratracheal instillation of bleomycin. The transverse slices at the level of the lungs show progression of the edema, inflammation, and fibrosis manifested by irregular regions of MR signal observed until day 11 (C) with trend to partial recovery on day 14 (D). MRI acquisition parameters include spin echo with repetition time = 500 ms, echo time = 16 ms, field of view = 70 mm, slice thickness = 1.2 mm, matrix = 256 × 256, acquisition time = 4.30 min.

Fixed tissue biopsies from the injection sites were provided by Neuroderm investigators and the extent of subcutaneous damage was evaluated by *ex vivo* MRH, which effectively identified the location of the injection and quantified the extent of subcutaneous necrosis and inflammation caused by the drug. Figure 8A shows *ex vivo* MRH of a cross section of the skin biopsy showing the damaged area confirmed with H&E histology (Figure 8B). The MIP of the 3-D rendered image of the whole tissue is shown in Figure 8C, with the segmented damaged area showed in red. Applying this method of MRH assessment on multiple tissues samples derived from different dose formulations provided a quantitative determination of relative irritancy of different injected formulations.

### *Rat embryo phenotyping: Cyclophosphamide model*

Conventional rat teratology studies typically include a cyclophosphamide-treated positive control. Cyclophosphamide exposure of pregnant rats causes hypoplasia of the prosencephalon and other cephalic defects, resulting in the hammerhead phenotype being expressed in embryos (Murphy 1962). The affected embryos have blunted tails, limb reductions, hypoplastic mandibular arches, and decrements in crown-rump length. In this article, we present an *ex vivo* MRH study performed in a rat study conducted at RTC (Rome, Italy) to identify birth defects. For this purpose, cyclophosphamide-exposed and negative control rat embryos from gestation day 20 were fixed in Bouin's fixative for 10 days and then transferred to 70% ethanol. Embryos were immersed in fluorinert (Fluorinert FC, 3M, USA) for whole embryo scanning. MRH of fixed normal (Figure 9A) and treated (Figure 9B) specimens was performed. The 3-D digital MRIs identified cephalic defects leading to the hammerhead phenotype, blunted tails, limb reductions, mandibular arches, and decrements in crown-rump length, all expected birth defect in cyclophosphamide-exposed embryos (Figure 9B). In addition, organ segmentation and volume calculations of main organs were obtained (Figure 9C). As such, *ex vivo* MRH can be a useful tool for phenotyping rat embryos where structural

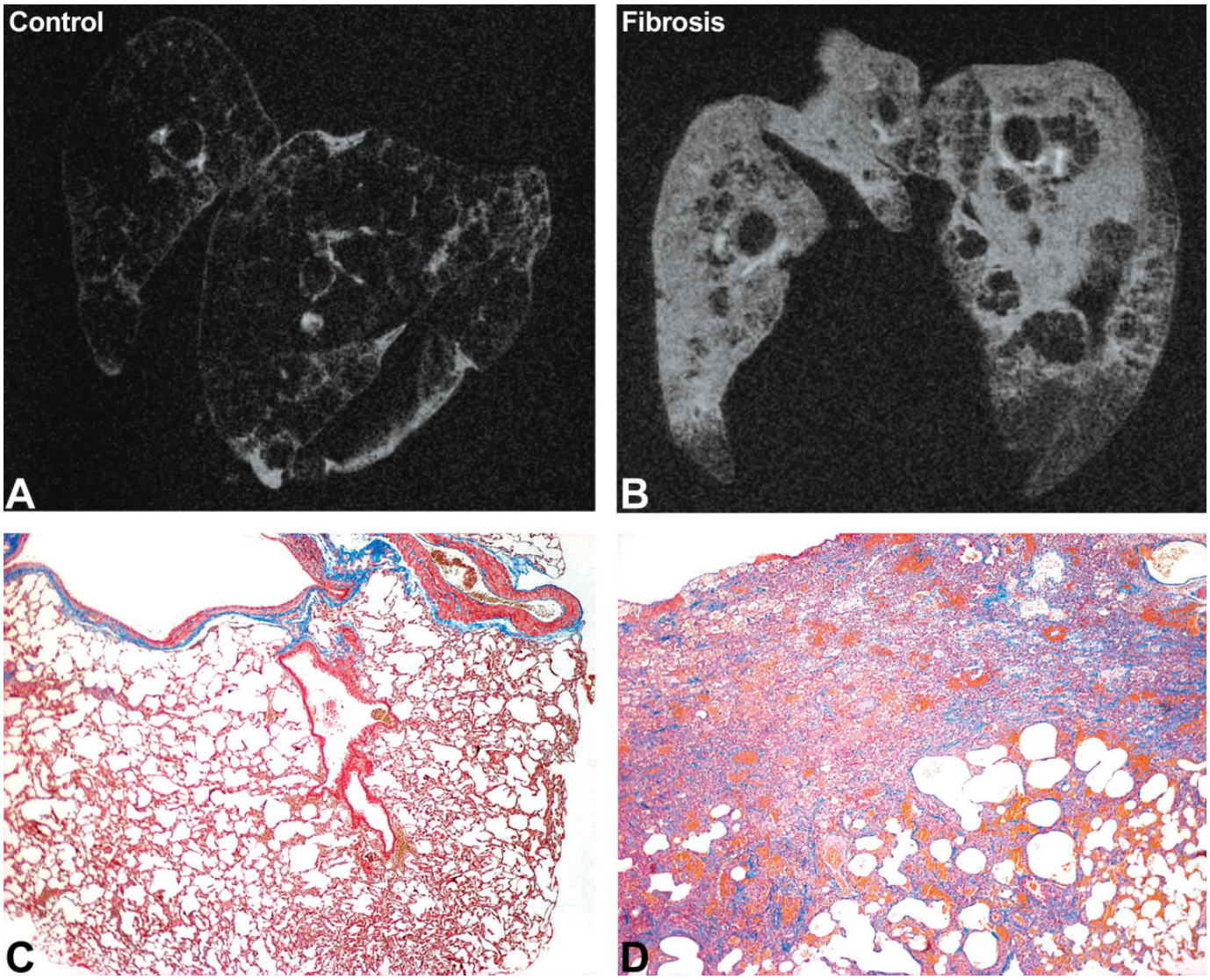


FIGURE 11.—*Ex vivo* magnetic resonance histology (MRH) and hematoxylin and eosin (H&E) histopathology of lung edema, inflammation, and fibrosis in rats. *Ex vivo* MRH of control (A) and fibrotic (B) lung inflated with air and immersion fixed in formalin. Note the increased bright signal in the affected lung indicating combined inflammation and fibrosis. Magnetic resonance imaging (MRI) acquisition parameters include gradient echo with repetition time = 50 ms, echo time = 7 ms, flip angle = 80°, field of view = 25 mm, slice thickness = 0.3 mm, matrix = 300 × 300, and acquisition time = 133 min. Histopathology staining by Masson's Trichrome of the control (C) and fibrotic (D) lung 11 days following the administration of bleomycin. The fibrosis is highlighted by the blue staining.

alteration can be identified and organ and tissue volumes can be quantitatively measured, leaving the sample intact for subsequent conventional pathology evaluation. In addition, *in vivo* MR assessments can also be performed to monitor and quantify changes in the phenotypes in utero and a preceding step to performing *ex vivo* assessments of the same organs.

### *Pulmonary fibrosis*

Pulmonary edema, inflammation, and fibrosis are the major component of chronic obstructive pulmonary disease (COPD) that in 2011 affected 12.4 million US adults, resulting in significant mortality (American Lung Association, August 2013 COPD Fact Sheet). An experimental preclinical model of pulmonary edema, inflammation, and fibrosis (Harlan Biotech, Israel) was obtained by single intratracheal installation of bleomycin into 6-week-old Sprague-Dawley rats. Performing MRI on lung tissue is particularly challenging since the air spaces in expanded bronchi, bronchioles, and alveoli do not provide a signal for MRI. Furthermore, expanding the lungs with fixative fluid, a routine technique, would provide an overly strong *ex vivo* MRH signal that would preclude detection of pulmonary edema, inflammation, and fibrosis. As such, lungs were inflated with air, the trachea was tied to prevent collapse, and the air-inflated lungs were then placed in fixative for 24 hrs. *In vivo* MRI of the rats was performed everyday for 2 weeks (Figure 10) and then *ex vivo* MRH was performed on air-inflated fixed lungs (Figure 11). Repeated *in vivo* MRI on the

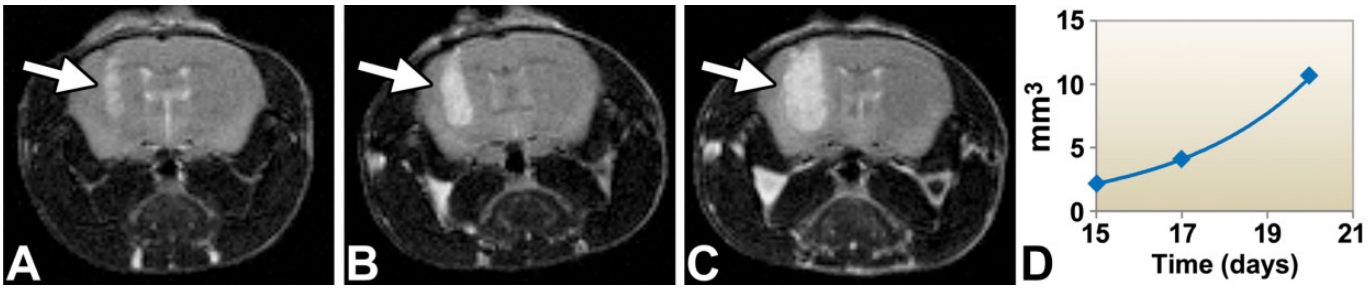


FIGURE 12.—*In vivo* magnetic resonance imaging (MRI) of brain tumors generated in CB6F1 mice. Axial view of the time course of tumor growth in a tumor-bearing mouse head by *in vivo* MRI. (A) 15, (B) 17, and (C) 20 days after cell injection. Growth quantification detected an exponential growth shown in the graph (D). MRI acquisition parameters include fast spin echo with repetition time = 2,500 ms, echo time = 74 ms, slice thickness = 1 mm, matrix = 256 × 256, field of view = 40 mm, and acquisition time = 13.2 min.

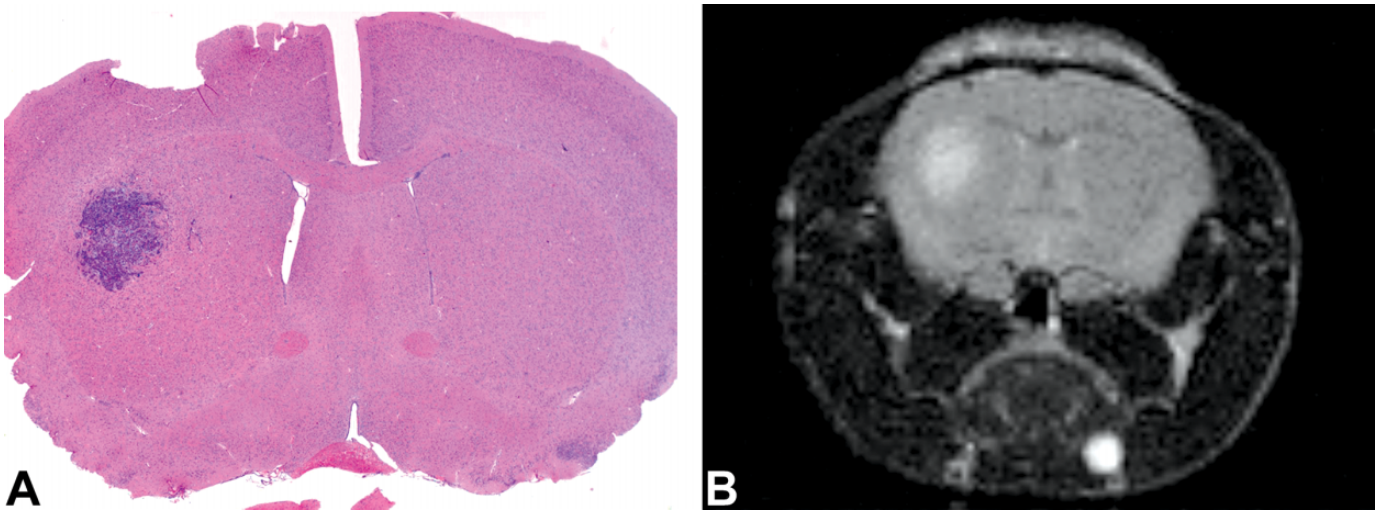


FIGURE 13.—Brain tumors—Histopathology and magnetic resonance imaging (MRI). (A) Hematoxylin and eosin (H&E) histopathology and (B) *ex vivo* MRI of a brain tumor 15 days after cell injection. MRI acquisition parameters include fast spin echo with repetition time = 2,500 ms, echo time = 74 ms, slice thickness = 1mm, matrix = 256x256, field of view = 40 mm, and acquisition time = 13.2 min.

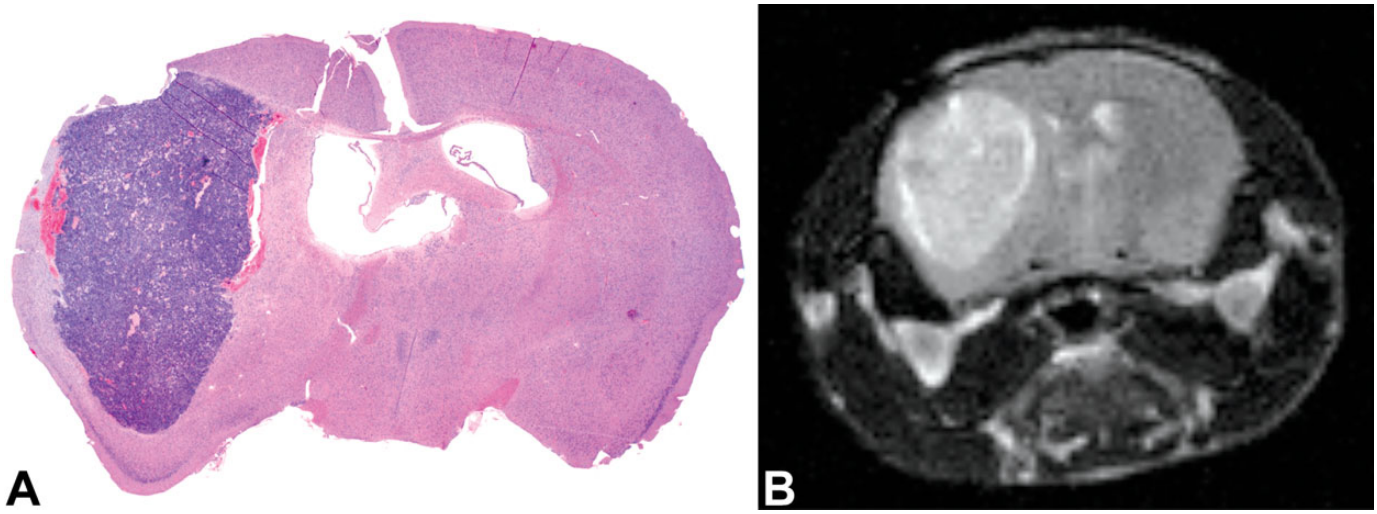


FIGURE 14.—Brain tumors—Histopathology and magnetic resonance imaging (MRI). (A) Hematoxylin and eosin (H&E) histopathology and (B) *ex vivo* MRI of a brain tumor 20 days after cell injection. MRI acquisition parameters includefast spin echo with repetition time = 2,500 ms, echo time = 74 ms, slice thickness = 1mm, matrix = 256x256, field of view = 40 mm, and acquisition time = 13.2 min.

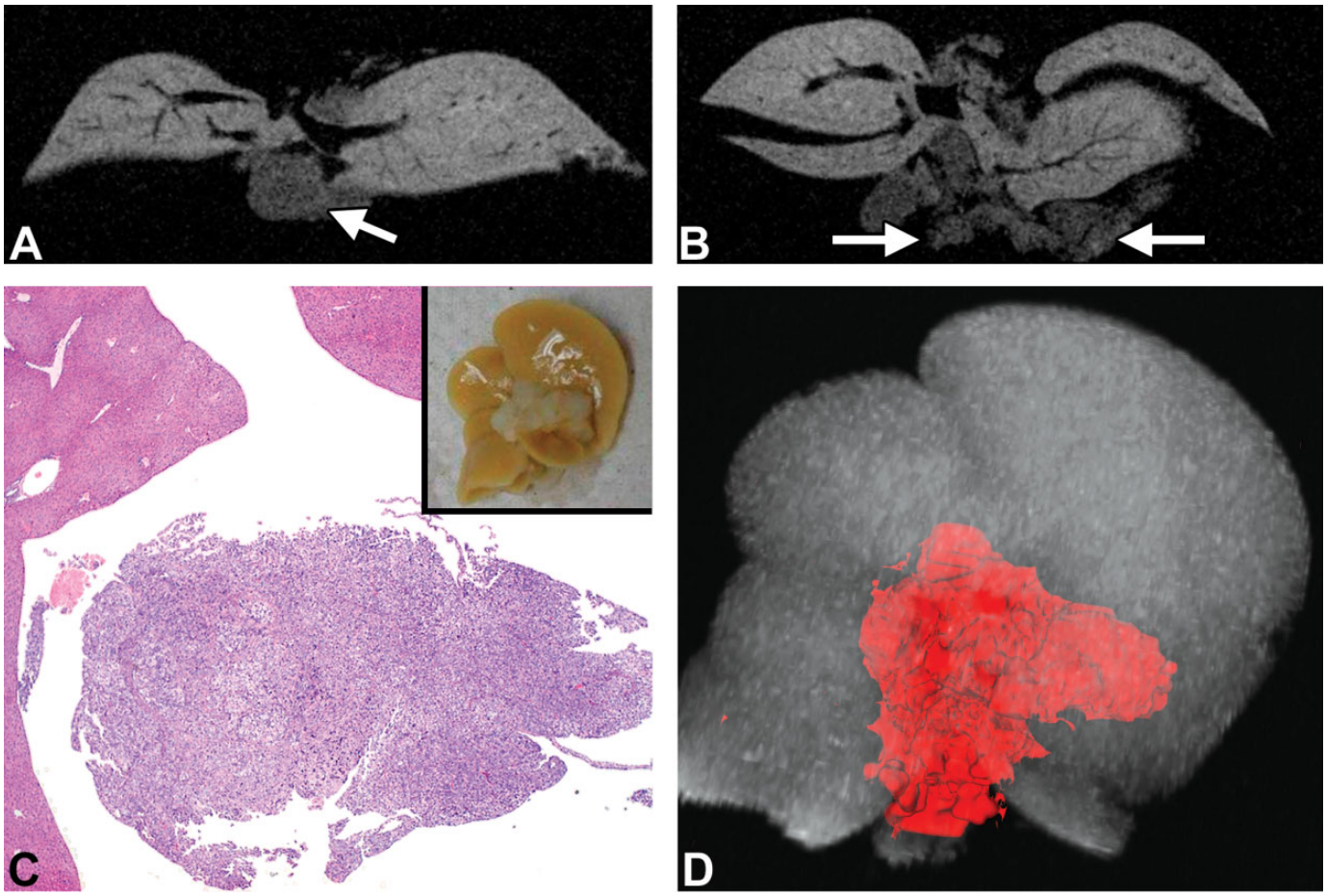


FIGURE 15.—*Ex vivo* magnetic resonance imaging (MRI) of liver and adjacent ovarian tumor. (A–B) Different MR slices showing the irregular appearance of the ovarian tumor attached to the ventral surface of the liver (arrows). (C) Hematoxylin and eosin (H&E) histopathology of tumor adjacent to the liver. The inset shows the formalin-fixed macroscopic view of the white appearance of the tumor adjacent to the liver. (D) 3-Dimensional (3-D)-rendered MRI image, reconstructed from all 128 individual 2-dimensional (2-D) slices, showing the segmented tumor in red having a volume of 102.477 $mm^3$.

same animal allowed longitudinal tracking of the progression and regression of the interstitial space occupying pathological processes (Figure 10A–D) manifested as a bright signal on top of the black background. *Ex vivo* MRI (Figure 11A, B) in combination with conventional histology (Figure 11C, D) provided a cross-correlated quantitative assessment of the components of interstitial thickening. Based on the ability to longitudinally monitor and ultimately quantify the extent of interstitial disease, compact MRI in combination with conventional histopathology allows different treatments to be compared for their therapeutic effectiveness.

### *Transplantable brain and ovarian tumor models*

Transplanting malignant cells into mice is a common approach to test potential anticancer chemotherapeutic agents (Killion, Radinsky, and Fidler 1999; Kerbel 1999). We used MRI in combination with conventional histopathology to monitor and quantitate the growth of transplantable tumor cells. CB6F1 mice at Hadassah Hebrew University Medical Center (Jerusalem, Israel) were anesthetized and Gl-261 murine glioma cells suspension ($10^5$ cells) were stereotactically injected using a Hamilton syringe (21 G) into the right brain hemisphere (0.6 mm anterior, 2.3 mm lateral to bregma at 3 mm depth from the dura). Tumor growth was noninvasively followed by *in vivo* MRI of injected mice for 20 days following cell injection (Figure 12). Tumor volume was measured noninvasively over time and found to have exponential growth. Moreover, *in vivo* MRI showed the variability in tumor size and location obtained for different animals, demonstrating the importance of longitudinal studies in the same animal rather than relying on statistics from groups of animals sacrificed at different intervals after injection. *Ex vivo* MRI of the cardiac-perfused mouse head confirmed the *in vivo* data and correlated well with histopathology (Figures 13 and 14).

An ovarian tumor model (Harlan Biotech, Israel) was induced by intraperitoneal injection of SKOV-3 cells into BALB/c nude mice. In this model, the injected tumor cells typically localize at the liver hilus, forming an irregular solid tumor mass (Figure 15A and B). Quantitation of tumor volume is an

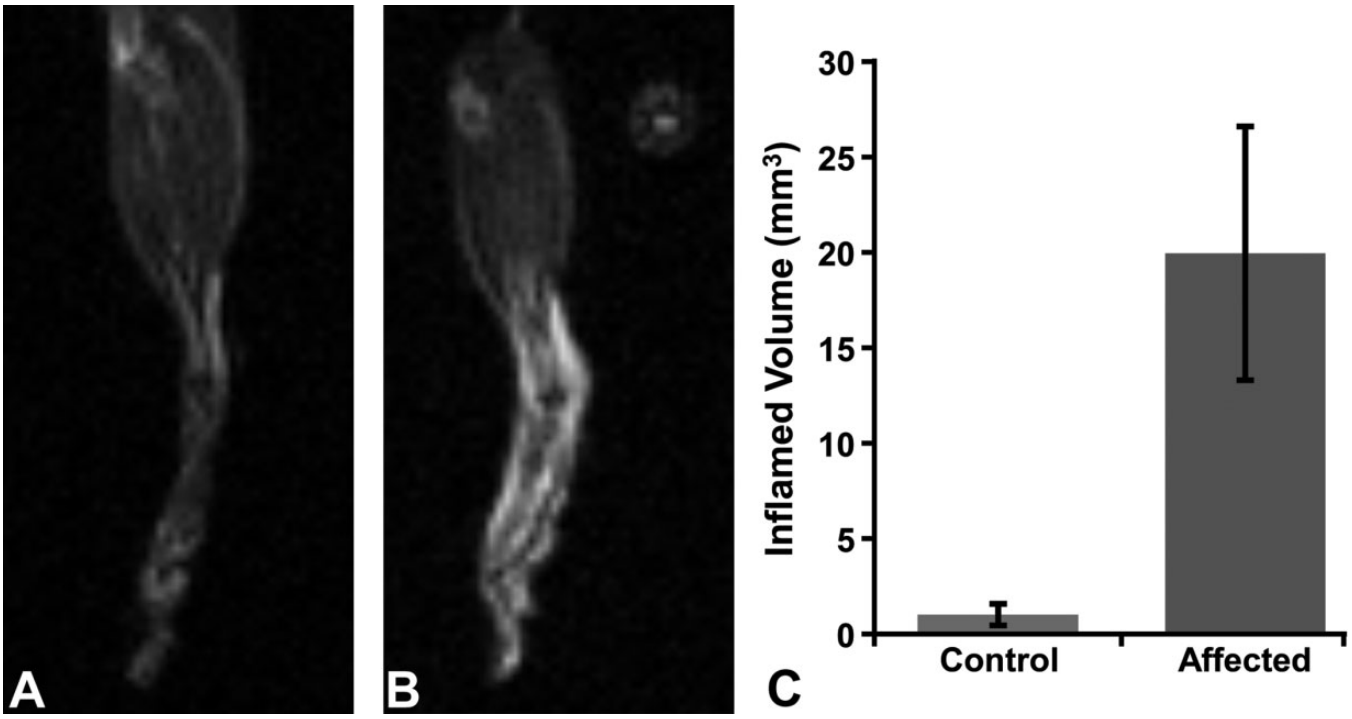


FIGURE 16.—*In vivo* magnetic resonance imaging (MRI) of mouse leg arthritis (synovitis) induced in BALB/c mouse. Predose *in vivo* MRI (A) and 10 days after induced arthritis (B) in the mouse leg. Note the bright signal in the inflamed region. The signal is increased in the affected leg as shown in the graph at the right, $n = 5$ (C). MRI acquisition parameters include fast spin echo with repetition time = 1,600 ms, echo time = 80ms, slice thickness = 1 mm, matrix = 200 × 192, field of view = 80 mm, and acquisition time = 5.5 min.

important metric to permit testing of potential anticancer chemotherapeutics. MRI is especially useful in quantification of irregular neoplastic growth, thereby providing an important adjunct to conventional histopathology (Figure 15C). The resulting irregular tumor appeared on the ventral surface of the liver having a volume of 102.477 $mm^3$ (Figure 15D). The model presented here demonstrates the ability of using *ex vivo* MRI for quantification of irregular neoplastic lesions, and by this, testing the efficacy of antineoplastic drugs which is not practical by other methods. These two tumor models demonstrate the ability of using M2 compact MRI for longitudinal studies in testing efficacy of anticancer drugs.

### *Mouse arthritis model (synovitis)*

Osteoarthritis occurs in more than 60% of people over the age of 65 and is second only to cardiovascular disease as a cause of morbidity in Western society (Cooper 1995; Wang 2008). Mouse models are commonly used in arthritis/synovitis research, and in this study we used the M2 compact MRI system as an adjunct to conventional histopathology. BALB/c mice were given single intravenous injection of a commercially available monoclonal antibody cocktail and 72 hrs later, mice were given an intraperitoneal injection of lipopolysaccharide (LPS; Harlan Biotech, Israel). Both *in vivo* (Figure 16) and *ex vivo* (Figure 17) MRI scans of the mouse legs detected synovitis and allowed longitudinal identification and quantitation of degrees of synovial inflammation manifested as enhanced signal intensity in T2-weighted images, over a 14-day period. In this monoclonal antibody–induced arthritis model, *in vivo* and *ex vivo* MRI was useful in identifying and quantifying the degree of inflammation with excellent correlation between *ex vivo* MRH images and conventionally stained histopathology sections (Figure 17).

### *Stroke*

Stroke is the fourth leading cause of death in the United States, affecting approximately 15 million people worldwide yearly. Here we use *in vivo* MRI and *ex vivo* MRH of two ischemic rat stroke models: the photothrombosis model (Prof. A. Friedman, Ben Gurion University, Israel) and the 4-vessel occlusion model (MD Biosciences, Israel). For the photothrombosis model, Rose Bengal (7.5 mg/ml in saline) was intravenously administered followed by exposure to halogen light, leading to stroke in the cortical area (Watson et al. 1985; Prager et al. 2009; Lapilover et al. 2012). *In vivo* and *ex vivo* MRI (Figure 18A and B) showed good correlation in localization and extent of damage detected. In the four-vessel occlusion model (Meilin, Machicao, and Elmlinger 2014), the vertebral and common carotid arteries were occluded to cause transient forebrain ischemia, resulting in massive loss of neuronal tissue in the caudate/putamen area (Figure 18C). As with other models described earlier, *in vivo* MRI allows longitudinal monitoring of lesion progression, while *ex vivo* MRH permits more definitive identification and

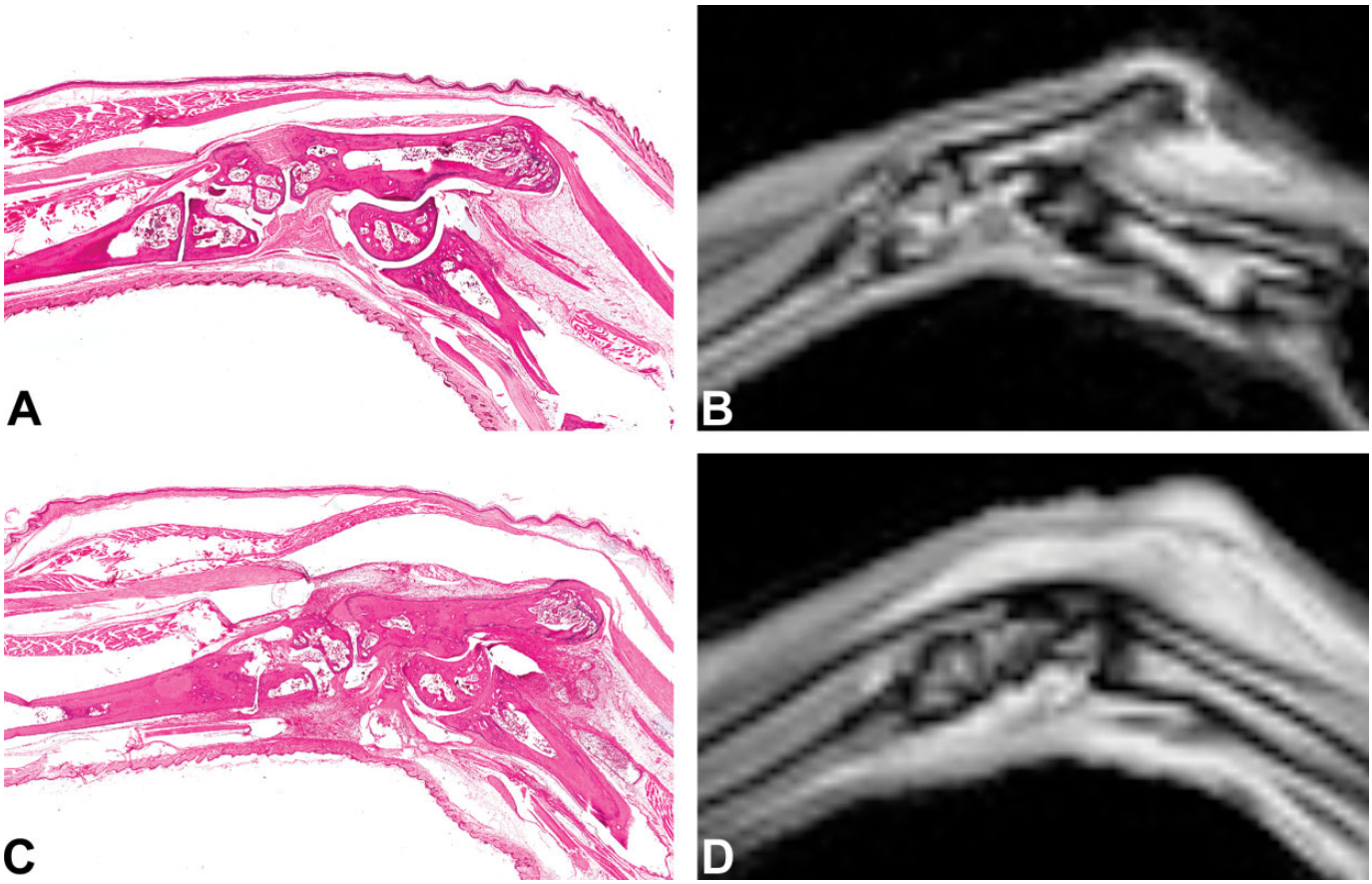


FIGURE 17.—*Ex vivo* magnetic resonance imaging (MRI) and histopathology of mouse leg arthritis (synovitis) induced in BALB/c mice. Histopathology (A) and *ex vivo* MRI (B) of control mouse leg showing normal anatomy. Histopatholgy (C) and *ex vivo* MRI (D) of a mouse leg 10 days after induction of arthritis. The acute inflammation of the synovial membrane correlates with the bright signal in the same areas in the MRI image. MRI acquisition parameters include fast spin echo with repetition time = 2,000 ms, echo time = 40 ms, slice thickness = 0.5 mm, matrix = 256 × 256, field of view = 40 mm, and acquisition time = 55 min.

quantification of lesion dimensions. Thus, the combination of MRI and MRH provide useful tools to monitor and quantitate effects of therapeutic intervention.

## DISCUSSION

Past use of MRI for imaging small animals has been limited to large imaging and research centers that could afford to acquire, maintain, and staff costly superconducting MRI systems and support the associated complex infrastructure as well as operate the technically sophisticated software and instrumentation. These centers have successfully leveraged MRI to produce exquisite high-resolution *in vivo* and *ex vivo* images with the trade-off of long acquisition times and low sample throughput (Johnson, Badea, and Jiang 2011; Xie et al. 2012). The advent of M2 compact MRI enables researchers and pathologists with no imaging or MRI experience to now be able to access and successfully leverage the powerful 3-D morphological and molecular imaging capabilities of MRI without the cost, complexity, and safety issues traditionally associated with superconducting MRI systems. The M2 MRI system efficiently provides *in vivo* images of rats and mice in a few minutes as well as *ex vivo* images of fixed specimens, which can be automated and provide higher resolution for 3-D reconstruction and quantitative measurement of tissue and lesion volume. Since the modality is noninvasive and the fixed specimen remains intact, conventional histopathology processing and evaluation can be carried out on the same samples following compact MRI. As such, M2 compact MRI can be highly complementary to conventional pathology providing additional morphological and quantitative indications of possible pathologies and toxicological effects. Using a variety of experimental toxicology models, we have shown the utility of this high-performance MRI platform for *in vivo* imaging as well as for high-resolution *ex vivo* 3-D MRH, with strong correlation to conventional H&E histology. *In vivo* MRI provides invaluable functional, morphological, and quantitative information of disease progression and regression by noninvasively imaging the same animals over time. Nondestructive *ex vivo* MRH provides high-throughput and high-resolution 3-D digital data sets of intact organs, with important morphological and quantitative information. With a high degree of correlation to conventional

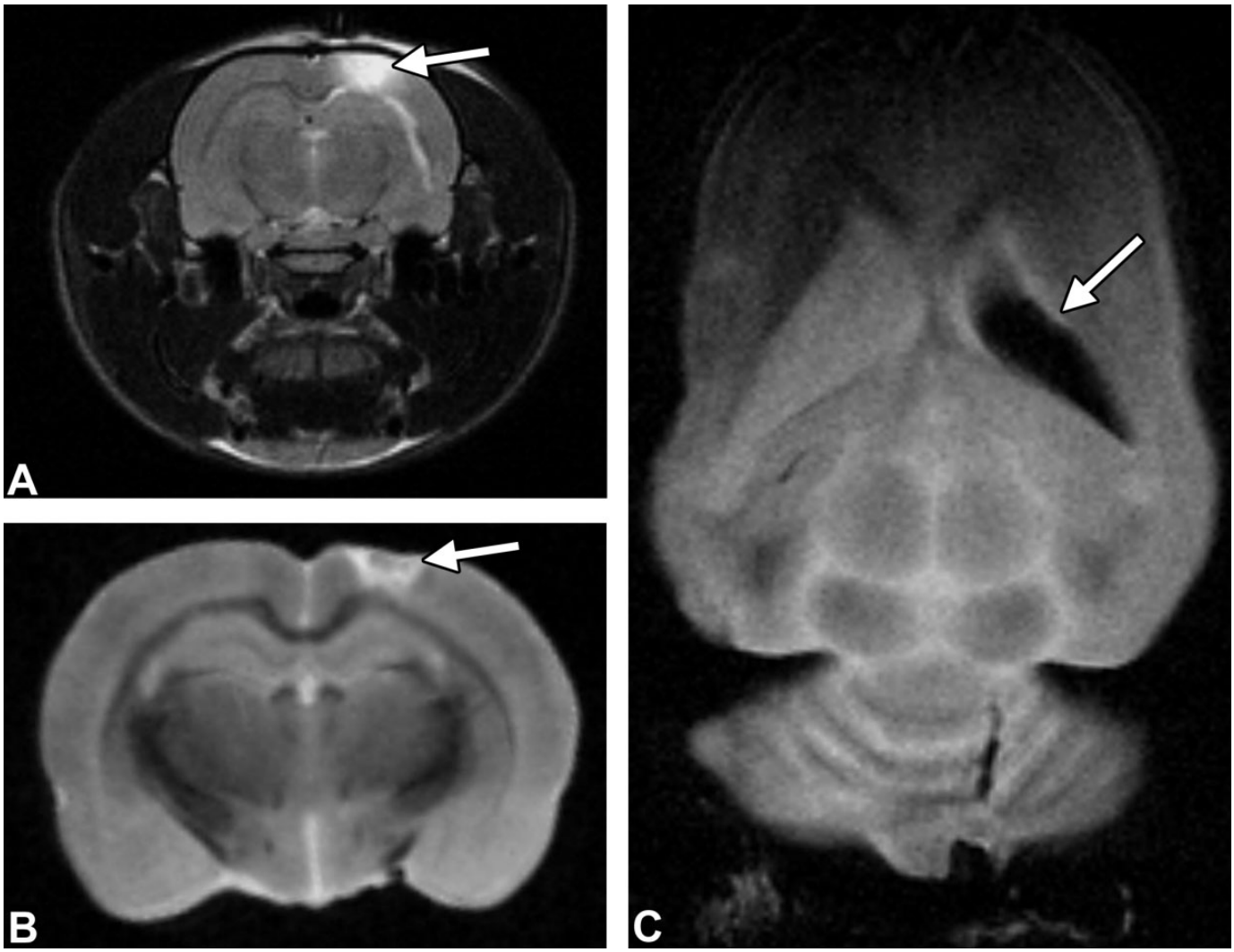


FIGURE 18.—Rat brain stroke. (A) *In vivo* and (B) *ex vivo* magnetic resonance imaging (MRI) of stroke induced in rat brain by photothrombosis showing the lesion in the cortical region. The infarction is distinguished by the bright signal (arrow). Good correlation is observed by *in vivo* and *ex vivo* MRI with respect to location and extent of damage. MRI (*in vivo*) acquisition parameters include fast spin echo with repetition time = 3,400 ms, echo time = 74 ms, slice thickness = 1 mm, matrix = 256 × 256, = field of view = 50 mm, and acquisition time = 16.5 min. MRI (*ex vivo*) acquisition parameters include fast spin echo with repetition time = 3,197 ms, echo time = 60 ms, slice thickness = 0.7 mm, matrix = 256 × 240, field of view = 30 mm, and acquisition time = 66 min. (C) *Ex vivo* MRI of rat brain induced by 4-vessel occlusion distinguished by the dark region (arrow) reflecting massive loss of neural tissue in the caudate/putamen area due to the infarction. MRI acquisition parameters include fast spin echo with repetition time = 3,000 ms, echo time = 60 ms, slice thickness = 0.7 mm, field of view = 30 mm, matrix = 256 × 256, and acquisition time = 61 min.

H&E, 3-D MR-based histology can provide additional insights into disease pathology as well as directing conventional histology to ensure key targets are fully assessed, considered, and quantitated in toxicological workups.

## AUTHORS' NOTE

This report is based on a presentation entitled "Practical Application of MRI Histology in Toxicological Pathology" presented at the annual meeting of the STP (Society of Toxicological Pathology) in June 2013 in Portland, Oregon.

## AUTHOR CONTRIBUTION

Authors contributed to conception or design (CB, YS, AN, NE, IS, RA, RM); data acquisition, analysis, or interpretation (CB, YS, AN, NE, IS, RA, RM); drafting the manuscript (CB, YS, AN, RM); and critically revising the manuscript (YS, AN, NE, RA, RM). All authors gave final approval and agreed to be accountable for all aspects of work in ensuring that questions relating to the accuracy or integrity of any part of the work are appropriately investigated and resolved. CB and YS are equal contributors.

## REFERENCES


Bosch, X., Poch, E., and Grau, J. M. (2009). Rhabdomyolysis and acute kidney injury. *New England J of Med* **361**, 62–72.

Cooper, R. M. (1995). Rheumatoid arthritis is a common disease with clinically important implications for the airway. *J Bone Joint Surg Am* **77**, 1463–65.

De Feo, F., Jacobson, S., Nyska, A., Pagani, P., and Traverso, C. E. (2009). Histological biocompatibility of a stainless steel miniature glaucoma drainage device in humans: A case report. *Toxicol Pathol* **37**, 512–16.

Dixon, D., Johnson, G. A., Cofer, G. P., Hedlund, L. W., and Maronpot, R. R. (1988). Magnetic resonance imaging (MRI): A new tool in experimental toxicologic pathology. *Toxicol Pathol* **16**, 386–91.

Geninatti-Crich, S., Szabo, I., Alberti, D., Longo, D., and Aime, S. (2011). MRI of cells and mice at 1 and 7 tesla with Gd-targeting agents: When the low field is better! *Contrast Media Mol Imaging* **6**, 421–25.

Johnson, G. A., Thompson, M. B., Cofer, G. P., Campen, D., and Maronpot, R. R. (1989). Magnetic resonance imaging of hepatic neoplasms in rat. *Vet Pathol* **26**, 303–8.

Johnson, G. A., Benveniste, H., Black, R. D., Hedlund, L.W., Maronpot, R. R., and Smith, B. R. (1993). Histology by magnetic resonance microscopy. *Magn Reson Quar* **9**, 1–30.

Johnson, G. A., Badea, A., and Jiang, Y. (2011). Quantitative neuromorphometry using magnetic resonance histology. *Toxicol Pathol* **39**, 85–91.

Kerbel, R. S. (1999). What is the optimal rodent model for anti tumor drug testing? *Cancer Metastasis Rev* **17**, 301.

Killion, J. J., Radinsky, R., and Fidler, I. J. (1999). Orthotopic models are necessary to predict therapy of transplantable tumors in mice. *Cancer Metastasis Rev* **17**, 279–84.

Lapilover, E. G., Lippmann, K., Salar, S., Maslarova, A., Dreier, J. P., Heinemann, U., and Friedman, A. (2012). Peri-infarct blood-brain barrier dysfunction facilitates induction of spreading depolarization associated with epileptiform discharges. *Neurobiol Dis* **48**, 495–506.

Lester, D. S., Lyon, R. C., McGregor, G. N., Engelhardt, R. T., Schmued, L. C., Johnson, G. A., and Johannessen, J. N. (1999). 3-Dimensional visualization of lesions in rat brain using magnetic resonance imaging microscopy. *Neuroreport* **17**, 737–41.

Lester, D. S., Pine, P. S., Delnomdedieu, M., Johannessen, J. N., and Johnson, G. A. (2000). Virtual neuropathology: three-dimensional visualization of lesions due to toxic insult. *Toxicol Pathol* **28**, 100–04.

Loeffler, W., and Oppelt, A. (1981). Physical principles of NMR tomography. *Eur J Radiol* **4**, 338–44.

Maronpot, R. R., Sills, R. C., and Johnson, G. A. (2004). Applications of magnetic resonance microscopy. *Toxicol Pathol* **32** 42–8.

Mauad, T. H., Van Nieuwkerk, C. M., Dingemans, K. P., Smit, J. J., Schinke, A. H., Notenboom, R. G., Van den Bergh Weerman, M. A., Verkruisen, R. P., Groen, A. K., Oude Elferink, R. P., Van der Valk, M. A., Borst, P., and Offerhaus, G. J. A. (1994). Mice with homozygous disruption of the mdr2 P-glycoprotein gene. A novel animal model for studies of nonsuppurative inflammatory cholangitis and hepatocarcinogenesis. *Am J Pathol* **145**, 1237–45.

Meilin, S., Machicao, F., and Elmlinger, M. (2014). Treatment with Actovegin improves spatial learning and memory in rats following transient forebrain ischaemia. *J Cell Mol Med*, **18**, 1623–30.

Milman, Z., Heyman, S. N., Corchia, N., Edrei, Y., Axelrod, J. H., Rosenberger, C., Tsarfati, G., and Abramovitch, R. (2013). Hemodynamic response magnetic resonance imaging: application for renal hemodynamic characterization. *Nephrol Dial Transplan*t **28**, 1150–6.

Morgan, B., Horsfield, M. A., and Steward, W. P. (2004). The role of imaging in the clinical development of antiangiogenic agents. *Hematol Oncol Clin North Am* **18**, 1183–206.

Murphy, M. L. (1962). Teratogenic effects in rats of growth inhibiting chemicals including studies on thalidomide. *Clin Proc Child Hosp Dist Columbia* **18**, 307–22.

Northup, S. J. (1999). Safety evaluation of medical devices: US food and drug administration and international standards organization guidelines. *Int J Toxicol* **18**, 275–83.

Nyska, A., Skolnick, M., Ziv, G., and Gulkarov, A. (1994). Correlation of injection site damage and serum creatine kinase activity in turkeys following intramuscular and subcutaneous administration of norfloxacin nicotinate. *Avian Pathol* **23**, 671–82.

Nyska, A., Glovinsky, Y., Belkin, M., and Epstein, Y. (2003). Biocompatibility of the Ex-PRESS miniature glaucoma drainage implant. *J Glaucoma* **12**, 275–80.

Nyska, A., Schiffenbauer, Y. S., Brami, C. T., Maronpot, R. R., and Ramot, Y. (2014). Histopathology of biodegradable polymers: challenges in interpretation and the use of a novel compact MRI for biocompatibility evaluation. *Poly Adv Technol* **25**, 461–7.

Okner, R., Oron, M., Tal, N., Nyska, A., Kumar, N., Mandler, D., and Domb, A. J. (2009). Electrocoating of stainless steel coronary stents for extended release of paclitaxel. *J Biomed Mater Res A* **88**, 427–36.

Prager, O., Chassidim, Y., Klein, C., Levi, H., Shelef, I., and Friedman A. (2009). Dynamic in vivo imaging of cerebral blood flow and blood-brain barrier permeability. *Neuroimage* **49**, 337–44.

Ramot, Y., Rosenstock, M., Klinger, E., Bursztyn, D., Nyska, A., and Shinar, D. M. (2012). Comparative long-term preclinical safety evaluation of two glatiramoid compounds (glatiramer Acetate, Copaxone(R), and TV-5010, protiramer) in rats and monkeys. *Toxicol Pathol* **40**, 40–54.

Ramot, Y., Touitou, D., Levin, G., Ickowicz, D. E., Zada, M. H., Abbas, R., Yankelson, L., Domb, A. J., and Nyska, A. (2014) Interspecies differences in reaction to a biodegradable subcutaneous tissue filler: severe inflammatory granulomatous reaction in the Sinclair minipig. *Toxicol Pathol* pii: 0192623314534995. [Epub ahead of print].

Schmid, A., Schmitz, J., Mannheim, J. G., Maier, F. C., Fuchs, K., Wehrl, H. F., and Pichler, B. J. (2013). Feasibility of sequential PET/MRI using a state of-the-art small animal PET and a 1 T benchtop MRI. *Mol Imaging Biol* **15**, 155–65.

Schuh, J. C. L. (2008). Medical device regulations and testing for toxicologic pathologists. *Toxicol Pathol* **36**, 63–9.

Sills, R. C., Morgan, D. L., Herr, D. W., Little, P. B., George, N. M., Ton, T. V., Love, N. E., Maronpot, R. R., and Johnson, G. A. (2004). Contribution of magnetic resonance microscopy in the 12-week neurotoxicity evaluation of carbonyl sulfide in Fischer 344 rats. *Toxicol Pathol* **32**, 501–10.

Smith, M. A. (1985).The technology of magnetic resonance imaging. *Clin Radiol* **36**, 553–9.

Wang, Y. X. (2008). In vivo magnetic resonance imaging of animal models of knee osteoarthritis. *Lab Anim* **42**, 246–64.

Watson, B. D., Dietrich, W. D., Busto, R., Wachtel, M. S., and Ginsberg, M. D. (1985). Induction of reproducible brain infarction by photochemically initiated thrombosis. *Ann Neurol* **17**, 497–504.

Xie, L., Cianciolo, R. E., Hulette, B., Lee, H. W., Qi, Y., Cofer, G., and Johnson, G. A. (2012). Magnetic resonance histology of age-related nephropathy in the Sprague Dawley rat. *Toxicol Pathol* **40**, 764–78.